Electronic Supplementary Material (ESI) for Nanoscale.
This journal is © The Royal Society of Chemistry 2024

Supporting Information

Asymmetric contact-induced selective doping in CVD-grown bilayer WS_2 and its application in high-performance photodetection with ultralow dark current

Abdul Kaium Mia[1], M. Meyyappan[1], P. K. Giri[1,2,*]

[1]Centre for Nanotechnology, Indian Institute of Technology Guwahati, Guwahati 781039, India.

[2]Department of Physics, Indian Institute of Technology Guwahati, Guwahati 781039, India.

1. CVD of WS_2 flakes

Monolayer and bilayer WS_2 flakes were directly grown on SiO_2/Si substrates using a two-zone temperature-controlled chemical vapour deposition (CVD) system. Commercially procured tungsten oxide (WO_3) and sulfur powder from Sigma-Aldrich were used as precursors for the CVD of 2D WS_2 in a quartz tube-based horizontal muffle furnace, as depicted in Figure 1. The S and WO_3 precursors were loaded separately into two mini quartz tubes with an inner diameter of approximately 1 cm. Initially, 10 mg of WO_3 powder was placed at the center of the high-

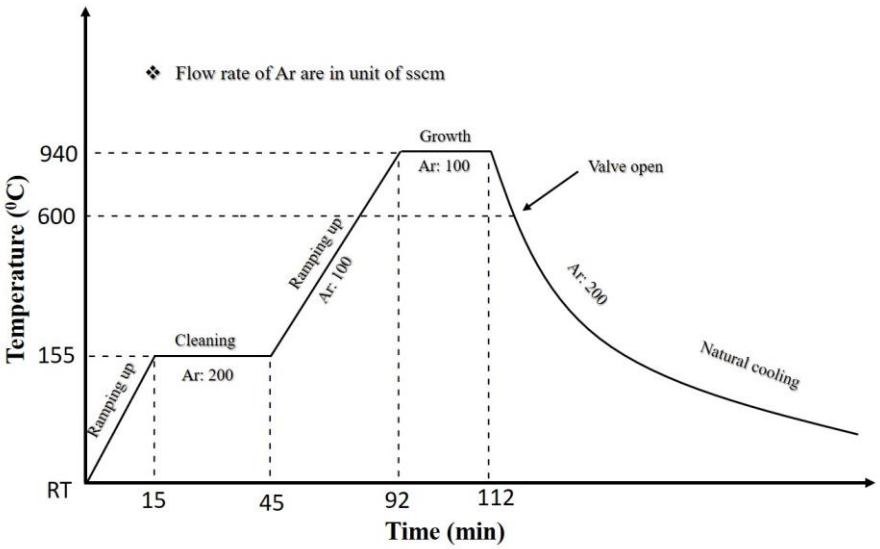

Figure S1. Temperature profile of the high-temperature zone with Ar carrier gas flow.

* Corresponding author, email: giri@iitg.ac.in

temperature heating zone of the furnace, with a few pieces of bare SiO_2/Si substrates placed just above the WO_3 powder, with their polished surfaces facing downward. Simultaneously, 200 mg of the S precursor was positioned in the middle of the low-temperature heating zone in the second mini quartz boat. These precursors were inside a one-side-closed quartz tube with a diameter of 2 cm. This one-side-closed tube enhances the precursors' vapor concentration near the substrate during the growth. High-purity argon (Ar) served as the carrier gas. This configuration ensures stable evaporation of the S and WO_3 sources at the appropriate temperatures and minimizes the risk of cross-contamination during WS_2 growth.

The temperature profile and carrier gas flow with time are shown in Figure S1. Initially, the quartz chamber was pumped down to a base pressure of 1.6×10^{-2} mbar before starting heating. The temperature in the second zone was then raised to 150°C over a span of 15 minutes. High-purity Ar with a flow rate of 200 sccm (standard cubic centimeters per minute) was introduced into the chamber and maintained at this temperature for 30 minutes, as shown in Figure S1 (temperature profile). The Ar flow removed any moisture and potential contaminants during this period. Subsequently, the temperature of the heating zone was increased to 940°C over 47 minutes with an Ar flow of 100 sccm. The temperature of the first zone was regulated so that it reached 150°C concurrently with the high-temperature zone reaching 940°C. At this juncture, the outlet valve was partially closed to achieve a pressure of 2.0 mbar in the CVD chamber. The system was then allowed to stabilize at this temperature for 20 minutes. Ar was used as the carrier gas during stabilization, flowing at a rate of 100 sccm at 2.0 mbar. After the growth process was completed, the system was allowed to cool naturally to room temperature. The outlet valve was opened once the temperature decreased to 600°C, and the Ar flow rate was increased to 200 sccm. Finally, the system was shut down when the temperature reached 300°C. With optimization of growth pressure to 1.2 mbar and a duration of 15 minutes, we observed a uniform monolayer growth, as depicted in Figure 1(a). We achieved maximum coverage with

bilayer WS_2, as demonstrated in Figure 1(c), by increasing the growth pressure to 2.0 mbar and extending the growth time to 20 minutes.

2. Transfer of WS_2 flakes from the growth substrate to the device substrate

The PMMA-assisted transfer process is illustrated schematically in Figure S2. Two distinct procedures were adopted: one involved heating at 120 degrees for 5 minutes, while the other remained unchanged for 24 hours after spin coating of PMMA. Mechanical damage was noted during the process that involved heating; optical images illustrating this damage can be seen in Figures S3(a) and S3(b). In contrast, Figure S3(c) displays the transferred film that underwent no heating; here, the flakes appear unchanged post-transfer, suggesting that the flakes undergo mechanical deformation due to thermal heating when PMMA is present. The low-magnification image of the transferred flakes on the SiO_2/Si substrate is shown in Figure S3(d), which reveals that almost all the flakes remain intact during this transfer process.

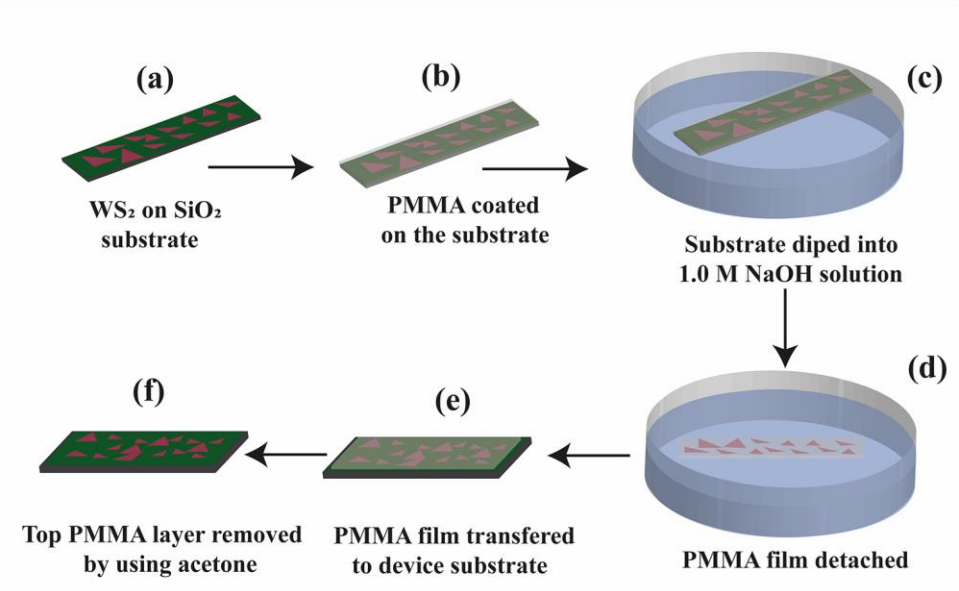

Figure S2. Schematic representation of WS_2 transfer process.

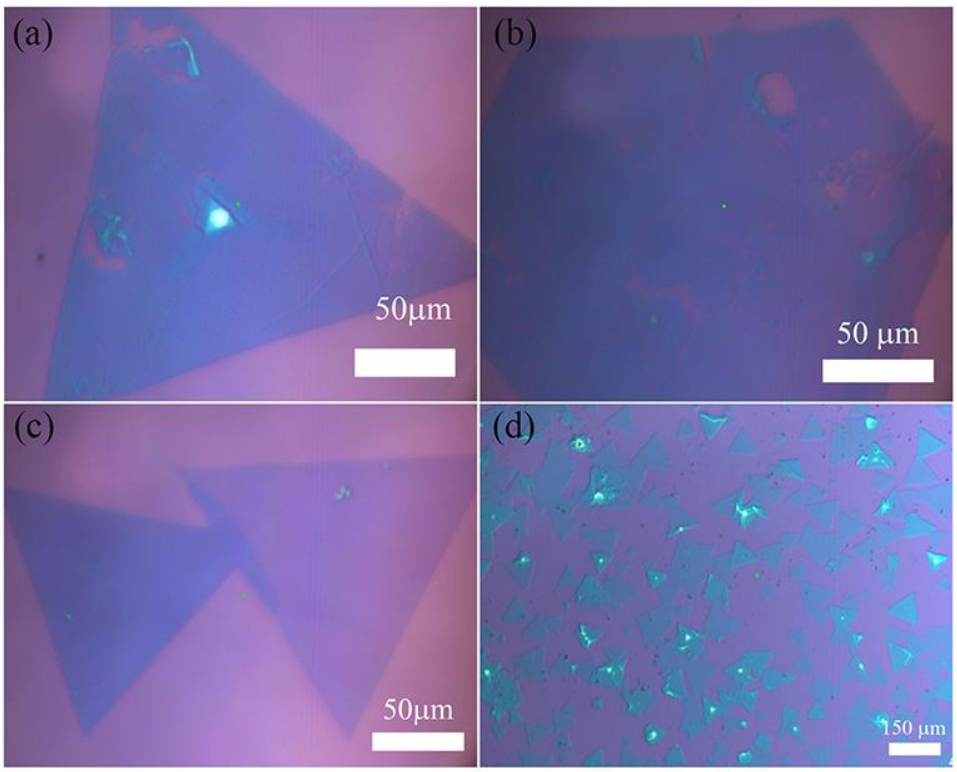

Figure S3. Optical images following two distinct transfer processes. (a, b) Heating-assisted transfer; (c) Transfer after PMMA coating without any heating; (d) Low-magnification image showing that all flakes remain unchanged after the transfer process that did not involve thermal heating.

The deconvoluted Raman spectra for the monolayer WS_2 before and after transfer are shown in Figure S4(a). The blueshift of the E_{2g} mode arises from the strain reduction from the transfer process. Raman spectra for monolayer and bilayer WS_2 under 488 nm laser excitation are shown in Figure S4(b). The two prominent peaks correspond to the E_{2g} and A_{1g} Raman modes, which represent the fundamental in-plane and out-of-plane vibrations, respectively. The separation between these peaks increases from 61.4 cm^{-1} to 62.8 cm^{-1} as the number of WS_2 layers changes from monolayer to bilayer.

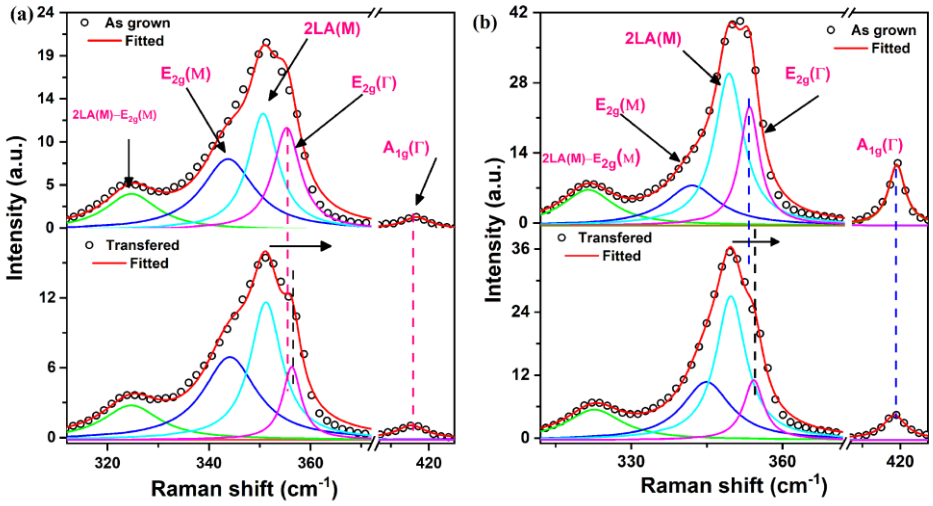

Figure S4. Comparative Raman spectra of WS_2 on SiO_2 substrate before and after transfer: (a) monolayer WS_2, (b) bilayer WS_2.

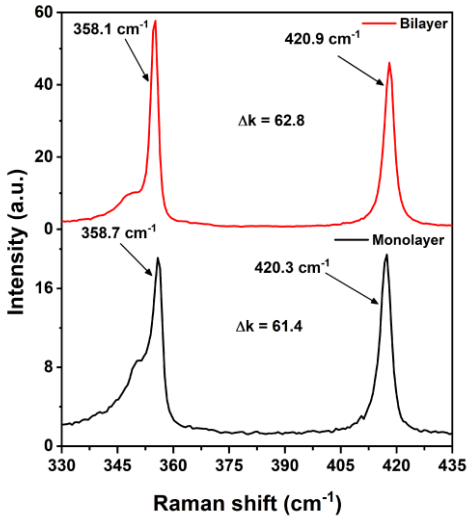

Figure S5. Raman spectra of monolayer and bilayer CVD grown WS_2 on SiO_2 substrate under 488 nm laser excitation.

The photoluminescence (PL) of monolayer WS_2 also confirms the strain reduction as the emission peak is blueshifted toward a lower wavelength, as shown in Figure S6.

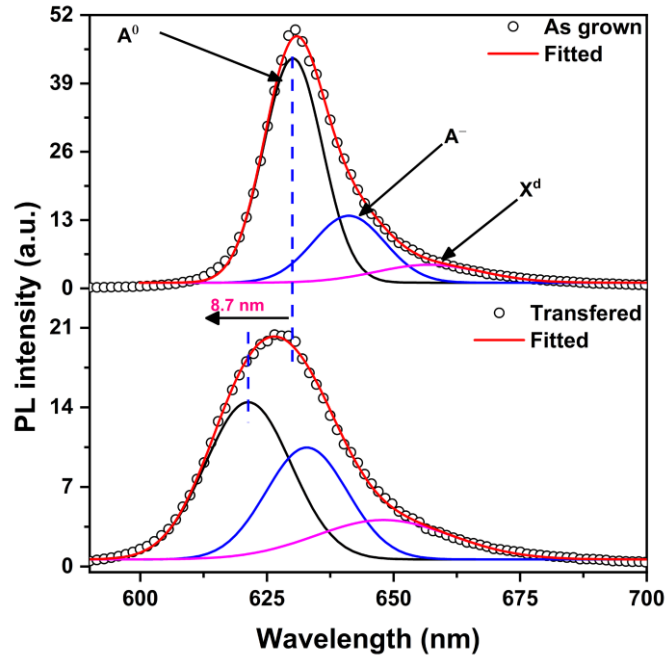

Figure S6. PL emission of monolayer WS_2 before and after transfer.

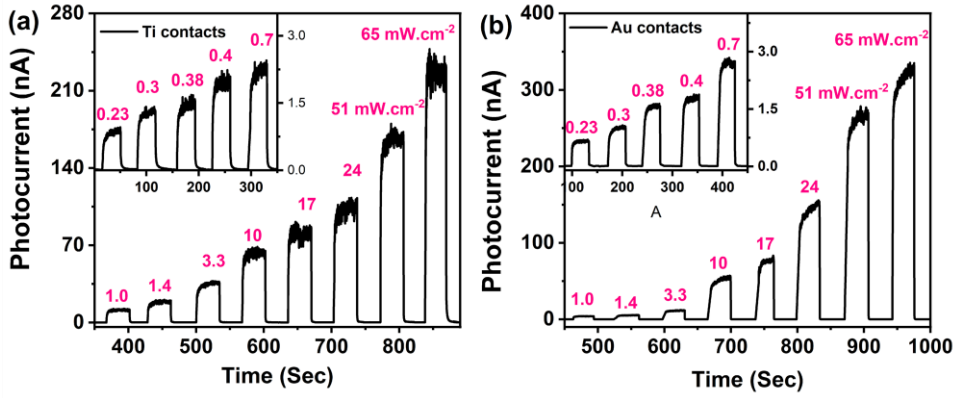

Figure S7. Photocurrent response of bilayer WS_2 PD with (a) symmetric Ti-Ti contacts and (b) symmetric Au-Au contacts under plused light illumination.

Monolayer WS_2-based photodetector performance:

The performance of monolayer WS_2-based PD with asymmetric contacts is shown in Figure S8. When compared to its bilayer counterpart, the lower electron mobility in monolayer WS_2 gives lower current values in the pA range.[1] The 4200 SCS parameter analyzer can measure currents down to the order of 10^{-15}A, so the current in the pA range is detectable. However, the instrument response time is relatively slow at this low current level. We have measured the response times by calculating the time difference of 90% of maxima and 10% of minima, as illustrated in Figure S8(f). This gives rise-time and decay time of 1.08 sec and 0.72 sec, respectively.

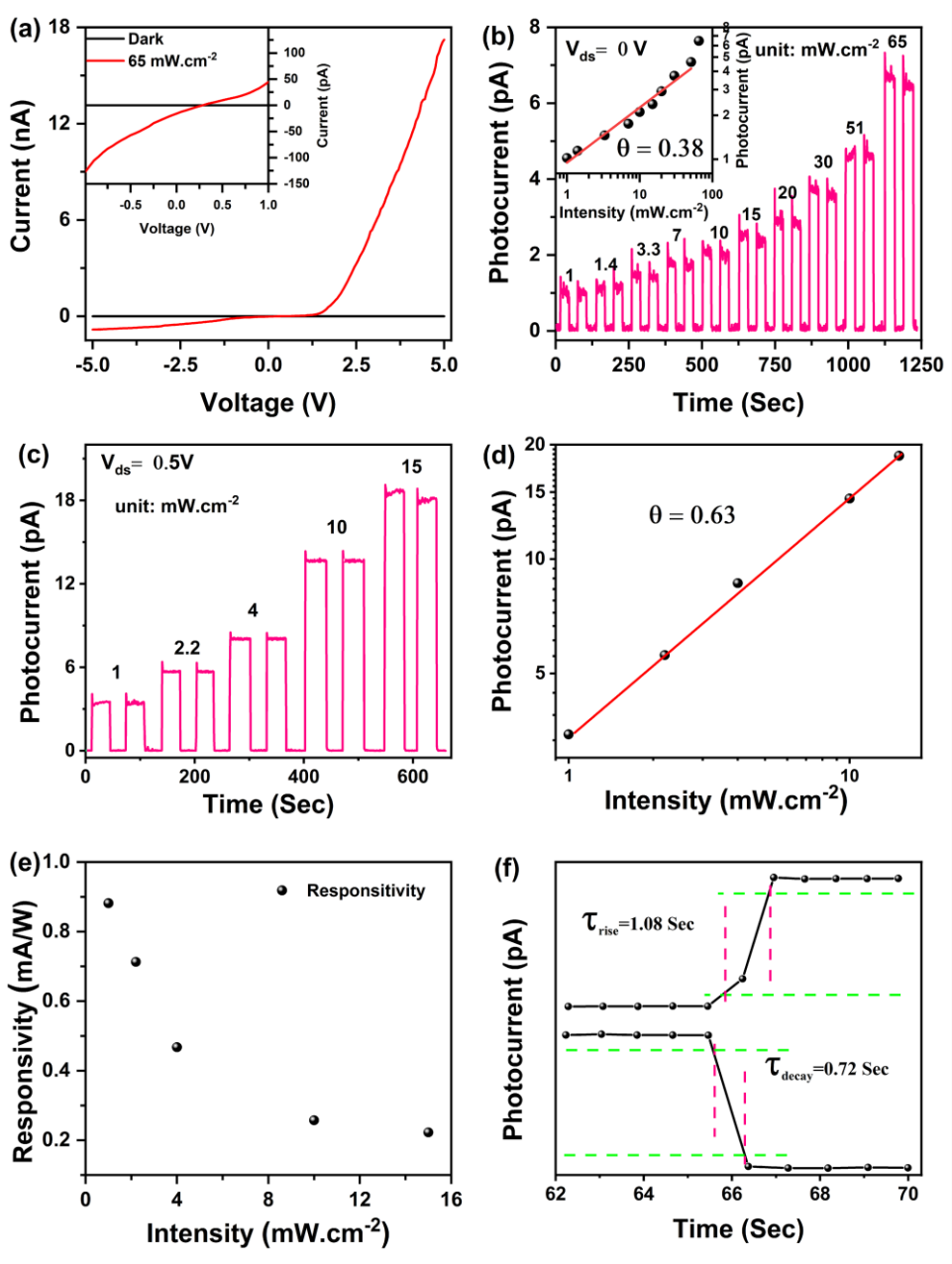

Figure S8. Photoresponse of monolayer WS_2-based asymmetric PD. (a) Pulsed response of monolayer WS_2 under 405 nm laser excitation. (b) Calibration curve between the photocurrent and laser intensity. (c) Variation of responsitivity with laser power. (d) Response time calculation.

Band alignment:

The Ti metal has a work function of 4.3 eV, lower than the n-type WS_2 (4.9 eV), forming an Ohmic junction. The Au metal has a work function of 5.1 eV higher than that of n-type WS_2, resulting in the formation of Schottky junction. Under the illumination condition, this band alignment facilitates the selective flow of electrons toward Ti, with hole movement towards Au. The field across the junction increases under the reverse bias and hence the efficient separation of photoinduced carriers.

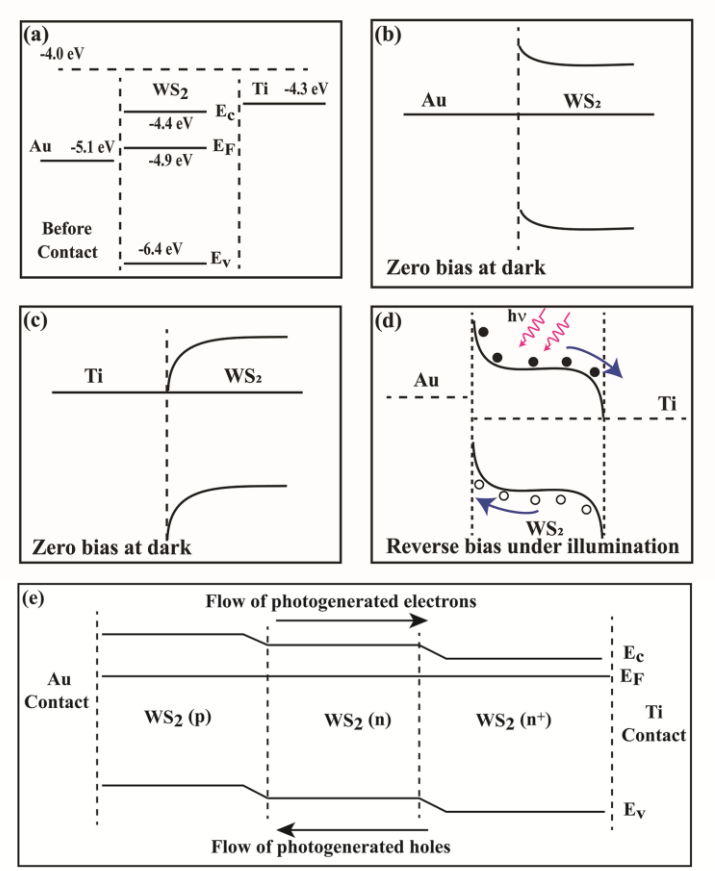

Figure S9. Energy band diagram of WS_2 with Au and Ti metal contacts: (a) energy band position of WS_2 and metals before contact. (b) Energy band diagram at Au/WS_2 interface after contact formation under zero bias at dark condition. (c) Energy band diagram at Ti/WS_2 interface after contact formation under zero bias at dark condition. (d) Energy band diagram under reverse bias with illumination after the formation of asymmetric Au/WS_2/Ti junctions. (e) Energy band diagram under zero bias showing the p-n-n^+ type junction due to the asymmetric contact induced doping in WS_2.

Reference:

1. D. Ovchinnikov, A. Allain, Y.-S. Huang, D. Dumcenco and A. Kis, *ACS Nano*, 2014, **8**, 8174–8181.